Pt Magnetic Polarization on Y_{3}Fe_{5}O_{12} and Magnetotransport Characteristics

Y. M. Lu, Y. Choi, C. M. Ortega, X. M. Cheng, J. W. Cai, S. Y. Huang, L. Sun, and C. L. Chien

Phys. Rev. Lett. **110**, 147207 — Published 5 April 2013

DOI: 10.1103/PhysRevLett.110.147207

Pt Magnetic Polarization on $Y_3Fe_5O_{12}$ and Magneto-Transport Characteristics

Y. M. Lu,[1] Y. Choi,[2] C. M. Ortega,[3] X. M. Cheng,[4] J. W. Cai,[1,*] S. Y. Huang,[5] L. Sun,[3,†] and C. L. Chien[5]

[1]*Beijing National Laboratory for Condensed Matter Physics, Institute of Physics, Chinese Academy of Sciences, Beijing 100190, China*

[2]*Advanced Photon Source, Argonne National Laboratory, Argonne, Illinois 60439, USA*

[3]*Department of Mechanical Engineering and Texas Center for Superconductivity (TcSUH), University of Houston, Houston, Texas 77204, USA*

[4]*Department of Physics, Bryn Mawr College, Bryn Mawr, Pennsylvania 19010, USA*

[5]*Department of Physics and Astronomy, Johns Hopkins University, Baltimore. MD 21218 USA*

Thin Pt films on yttrium iron garnet (YIG = $Y_3Fe_5O_{12}$) show ferromagnetic-like transport properties, which may impact the functionality of Pt in spin current detection, but do not provide direct quantitative information on the Pt magnetization. We report magnetic x-ray magnetic circular dichroism (XMCD) measurements of YIG/Pt(1.5 nm) showing an average Pt moment of 0.054 μ_B at 300 K and 0.076 μ_B at 20 K. This observation indicates strong proximity effects and induced magnetic ordering in Pt on magnetic insulators and their contribution to the spin-related measurements should not be neglected. The transport characteristics also suggest considerable modifications in the Pt electronic structure due to magnetic ordering.

PACS numbers: 75.70.-i, 75.25.-j, 75.47.Np, 72.25.-b

Spintronic phenomena exploit generation, manipulation, and detection of spin polarized charge carriers. Spin imbalance exists in magnetic materials where band structure splitting results in differences in effective mass, Fermi velocity, wave vector and density of states for spin-up and spin-down charge carriers [1-3]. Recently it has been demonstrated that, in addition to magnetic materials, spin imbalance can also be generated in non-magnetic materials by an external electrical field, magnetic field or thermal gradient. Even more significantly, one can now explore the effects of a pure spin current without the accompaniment of a charge current carrying a maximal spin angular momentum with minimal charge carriers [4-7].

Spin Hall effect (SHE) is among the first pure spin current phenomena, where a charge current in a non-magnetic material results in a pure spin current by the strong spin-orbit coupling (SOC) of the host. Direct SHE has been observed in a number of non-magnetic metals and semiconductors [1,2] and the resultant spin accumulation can be detected optically [3]. To electrically measure a pure spin current, one can use a lateral non-local spin valve [4,5] structure where a ferromagnetic component is placed within the spin diffusion length of only a few tens of nm from the current. In the inverse spin Hall effect (ISHE) [6,7], a non-magnetic metal with strong SOC can convert a pure spin current into charge accumulation. The prowess of converting a spin current to an electrical signal via the ISHE is specified by the spin Hall angle Θ_H [8,9], which is the ratio of the spin Hall conductivity and the charge conductivity. As in the case of its counterpart of charge Hall angle, the value of Θ_H can be of either sign. A number of metals with a large Θ_H have been measured experimentally. Some experimental values of Θ_H are consistent with calculated results, whereas others disagree even in sign.

Of all the non-magnetic metals, platinum (Pt) has been used most often as a pure spin current detector. Indeed, Pt is instrumental in establishing virtually all the pure spin current phenomena including the spin Seeback effect (SSE) [10,11], spin pumping [12], spin Hall switching [13], spin Hall induced ferromagnetic resonance [14]. In all of these cases there are magnetically ordered/non-magnetic (Pt) interfaces in generating, transporting and detecting the

spin currents. It is essential to determine if the non-magnetic metal in contact with a ferromagnetic material acquires ferromagnetic characteristics, or its unique role in converting pure spin current would be compromised. Thus it is of critical importance to ascertain the non-magnetic nature of spin current detectors, such as Pt, so that the magneto- and thermo-spin transport phenomena can be unequivocally established.

Recently, SSE in ferromagnetic insulators in the longitudinal geometry has been studied in details [15,16]. Since in this geometry the temperature gradient is along the spin current direction, one expects there should only be SSE without the presence of the anomalous Nernst effect (ANE), which contaminates the SSE in the transverse geometry. However, the YIG/Pt samples, where a Pt thin film has been grown on insulating ferrimagnetic $Y_3Fe_5O_{12}$ (YIG), unexpectedly show anisotropic magnetoresistance (AMR), anomalous Hall effect (AHE), and ANE behaviors. These ferromagnetic-like characteristics strongly suggest the presence of induced Pt magnetic moments, and from the Pt thickness dependence, Pt moments close to the YIG/Pt interface. However, these acute magnetic proximity effects notwithstanding, magneto-transport results do not provide direct and quantitative information on the Pt magnetization.

In this work, we report on direct Pt magnetic moment measurements using x-ray magnetic circular dichroism (XMCD)[17]. XMCD is an element specific technique that determines the induced magnetic moments in the Pt atoms. XMCD has been used previously to reveal Pt moments in contact with various conducting ferromagnetic surfaces and confirming the interfacial proximity behavior [18.19]. In the present case, we have observed clear temperature dependent ferromagnetic ordering in the Pt thin films grown on epitaxial YIG substrates. This observation provides a direct evidence of inducedmoment in Pt when it is in contact with magnetically ordered materials, either conducting (e.g., Fe, Co) as previously established or insulating (e.g., YIG) as reported here. The observed magnetic polarization in Pt due to proximity effect when in contact with a ferromagnetic metal or insulator questions the suitability of Pt as a pure current detector.

In this study, we used substrates that consist of 18 μm thick single crystalline (111) YIG layers grown by liquid phase epitaxy on (111) $Gd_3Ga_5O_{12}$(GGG) substrates. The YIG layers have a top surface root mean square roughness of less than 0.3 nm over an scanning area of 1×1 μm^2, as characterized by atomic force microscopy (AFM) (Fig. 1a). Full width at half maximum (FWHM) of the (444) peak rocking curve from these YIG is about 0.0116°, as measured on a Bruker D8 Discover x-ray diffractometer using Cu $K\alpha_1$ radiation. Patterned Pt thin films with thickness between 1.3 nm to 30 nm via a physical mask were sputter deposited on GGG/YIG samples. The samples for x-ray diffraction, XMCD and transport measurements have the dimension of 5×3×0.5 mm^3. To establish the close relationship between XMCD and the magneto-and thermal transport properties, specimens cut from the same sample have been used in various measurements.

Magnetic hysteresis loop measurements performed on a Quantum Design superconducting quantum interference device (SQUID) magnetometer show that the YIG films are magnetically soft and isotropic in the film plane. As shown in Fig. 1(b), at room temperature, YIG layer has an in-plane saturation field of about 60 Oe and a spontaneous magnetization ($4\pi M_S$) of 1.75 kG, which is revealed in the out-of-plane measurements due to the shape anisotropy. As shown in the inset of Fig. 1(b), the spontaneous magnetization of YIG increases monotonically with decreasing temperature and reaches 2.48 kG at 5 K. These magnetic properties agree well with those of bulk YIG.

XMCD measurements were performed on the 4ID-D beamline at the Advanced Photon Source at the Argonne National Laboratory using fluorescence detection mode at the Pt $L_{2,3}$ absorption edges ($2p_{1/2,3/2} \rightarrow 5d$ transition). Circularly polarized x-rays were generated using a 500 μm-thick diamond phase retarder, and XMCD was measured by switching the x-ray helicity. An electromagnet was used to generate external magnetic fields parallel to the sample surface and in the plane determined by the incident x-ray direction and the sample surface normal direction. X-ray incident angle is about 3 degree.

XMCD can provide direct magnetization measurement along the wave vector direction with element-specificity. XMCD characterization of Pt L_2 and L_3 edges was performed to probe the magnetization of Pt atoms on YIG. Contrary to the report by Geprägs *et al* [20], clear XMCD signal from Pt has been detected. Fig. 2a shows polarization-averaged x-ray adsorption spectra (XAS) and XMCD spectra for a 1.5 nm Pt film. The same scaling factor to normalize the XAS step height to 2.07 at the L_3 edge and 1.00 at the L_2 edge was used for the XMCD spectra [21]. Clear dichroism effect can be observed and the sign of the XMCD spectra changes with applied magnetic field direction. Also the XMCD signal intensifies when measurement temperature is lowered from 300 K to 20 K. It is known that the artifact signal in XMCD measurement has a lineshape similar to the 1st derivative of XAS. In the inset of Fig. 2b, the XAS derivative curves are plotted together with the XMCD results obtained at 20K. With opposite external fields, the artifact signal has identical lineshape, but different from XMCD. This difference confirms the presence of ferromagnetic ordering in the Pt film. In the inset, the XMCD data were plotted with error bars to indicate the noise level in measurements.

The Pt L_3 XMCD to XAS step edge height ratio is around 1% for this sample. This value is significantly lower than XMCD signals observed from Pt in contact with pure 3*d* ferromagnets. In comparison, in FePt nanoparticles, a 15% XMCD to XAS step edge height ratio was observed at the Pt L_3 [22]. For thin film structures, a 22% XMCD to XAS step edge height ratio was observed for a 0.15 nm Pt grown on Co. This ratio decreases to about 9 % and 4 % when Pt thickness has been increased to 1 nm and 2 nm, respectively. Assuming the Pt magnetization possesses an exponential decay from the Pt/Co interface, a decaying constant of 0.41 nm was reported [23]. Resonant magnetic x-ray reflectivity studied further suggested that the induced Pt moments are located within 1 nm from the Co/Pt interface [19]. In Ni/Pt multilayers, a layer-resolved XMCD study confirmed that the induced Pt moment was localized near the Ni/Pt interfaces [23]. The lower value of observed XMCD signal strength from Pt grown on YIG is a direct reflection of the smaller magnetization in YIG.

Further investigation using the sum rules [24,25] allows the determination of per Pt atom orbital moment m_o and spin asymmetry term m_s+7m_T , including the spin moment m_s and the magnetic dipole moment m_T. We used the number of 5*d* holes of n^{Pt}_h=1.73 as done for FePt[24]. For the two measurement temperatures of 300 K and 20 K, m_o has been determined to be 0.010 μ_B and 0.017 μ_B, and the effective spin moment m_s+7m_T has been determined to be 0.044 μ_B. In Co/Pt bilayers, the $7m_T$ term was about one order of magnitude smaller[23]. An increase of average Pt moment from 0.054 μ_B at 300 K to 0.076 μ_B at 20 K is recorded as the YIG magnetization changes from 1.75 to 2.48 kG. The fast increase in Pt moment could reflect the significant magnetization change in YIG.

In addition to XMCD, it is essential to compare the resistivity, MR, thermo-galvanic as well as Hall effect for Pt thin films grown on YIG and GGG substrates. AMR effects can be clearly observed in the Pt films grown on YIG. Fig. 3 shows the representative geometry and thickness dependences of the MR and thermal effects in these samples. Such effects are absent from the GGG/Pt samples. The longitudinal and transverse MR of the YIG/Pt show the same field dependences as those of the hysteresis loops of YIG. Coupled with the AMR effect is the anomalous Nernst effect as shown Fig 3b shows the thermo voltage measured for YIG/Pt(4nm) with a temperature gradient applied perpendicular to the sample plane. The field dependence of the thermal voltage coincides with the sample AMR, both coupled to the magnetization of the film.

With the in-plane applied magnetic field exceeding the saturation field of YIG and rotating in-plane, the resistivity shows a $\cos^2\theta$ dependence, where θ is the angle between the field direction and the length direction of the Pt pattern (inset of Fig. 3b). Decrease in MR ratio with increasing film thickness (Fig. 3c) supports the argument that magnetic order in Pt deposited on YIG can be a result of the magnetic proximity effect.

A closer look at the temperature dependence of the magneto-transport properties of the Pt thin films shows different characteristics from conventional bulk ferromagnetic materials, i.e., the magnetoresistance has an initial increase with decreasing temperature from room

temperature , but the trend turns negative below 100 K (Fig. 4a). In addition, resistivity of the Pt thin film samples also shows significant thickness dependence. For films thicker than 10 nm, sample resistivity decreases gradually with temperature reduction. But non-monotonic temperature dependence becomes obvious when film thickness drops below 4nm. As shown in Fig. 4b, a resistivity minimum appears at around 20 K for the 1.5 nm Pt, 15 K for the 2 nm Pt and 10 K for 4 nm Pt, respectively. This occurrence of the metal to insulator transition in the Pt thin film sample should originate from the weak localization of electrons caused by dimensional effect. Any way, the slight resistivity increase for thin Pt layers at low temperature cannot account for the AMR reduction below 100 K.

The Pt film resistivity grown on GGG and YIG is compared. As shown in Fig. 4c, both series samples exhibit very similar thickness and temperature dependence. But under the otherwise same condition, GGG/Pt shows larger resistivity and this becomes more significant for thinner Pt layers. Considering the fact that the YIG underlayer and the GGG substrates have same surface roughness, the resistivity reduction of the Pt layers should not come from the thin film uniformity. The introduction of magnetic ordering in Pt by the YIG underlayer will result in the band split for the Pt 5*d* spin up and spin down electrons, which in turn will lower the density of states (DOS) at the Pt Fermi level. Reduction in DOS will result in less *s*-*d* scattering and lead to a smaller resistivity for the magnetic ordered Pt layer. Therefore, comparison between the Pt film resistivity of YIG/Pt and GGG/Pt also suggests that the electronic structure of the Pt layer has been appreciably modified by the YIG underlayer.

Besides AMR, the YIG/Pt samples possess both temperature sensitive ordinary (OHE) and anomalous (AHE) Hall effect. Since the temperature dependence of AHE in the YIG/Pt films has been discussed previously[20], we focus on the OHE in the samples. As shown in Fig. 4c, thinner Pt layers exhibit more prominent OHE temperature dependences. There is a change of OHE coefficient sign from negative at room temperature to positive at low temperatures. Phenomenologically, the OHE coefficient (R_H) and resistivity of a material can be related to charge carrier concentration and corresponding mobility as,

$$R_H = \frac{p\mu_p^2 - n\mu_n^2}{q(p\mu_p + n\mu_n)^2}$$

$$\rho = \frac{1}{q(n\mu_n + p\mu_p)}$$

where *p, n,* μ_p *and* μ_n are the hole, electron density and their mobility, respectively. With the possible existence of both charge carriers, it is impossible to determine their temperature dependences just from the OHE coefficient and resistivity data. But nonetheless, these measurements suggest that the electronic band structure can have significant change for thin Pt films and result in OHE coefficient increase and AMR reduction. Strong temperature OHE coefficient dependence can only be observed for samples on YIG substrates, not on the GGG substrates, and will diminish with increasing Pt thickness. These observations again indicate the significant interactions between YIG and Pt and interfacial nature of this interaction. Recent *ab initio* study explained the spin polarization mechanism in Pt on YIG [26]. Phenomenologically, we believe the interfacial electrons from Pt can penetrate into YIG and be reflected back into the Pt. Affected by the strong exchange interaction within YIG, spin splitting and appreciable change in the DOS at the Fermi level will happen in the interfacial Pt layers, thus lead to the observed thickness dependent Pt transport behavior. The details of phenomenon are currently under theoretical investigation and not the focus of this report.

In summary, well-defined XMCD peaks at the L adsorption edges of Pt and the inversion of dichroic signal with opposite magnetic fields, both at 300 K and 20 K, demonstrate a clear magnetic polarization and proximity effect in Pt thin films grown on ferromagnetic YIG. Using XMCD, average polarized Pt magnetization of 0.07 μ_B per Pt has been determined for a layer 1.5 nm thick. Pt moment orientation and temperature dependence show strong correlation to the YIG magnetization. Magneto-transport properties of YIG/Pt show thickness dependent ferromagnetic like behaviors that are absent in the GGG/Pt samples. The magneto-transport characteristics of thin Pt layers are also different from common uniform magnetic material, displaying unconventional AMR and OHE coefficient temperature dependences.

ACKNOWLEDGEMENTS

J.W.C. is in debt to Dr. X.-G Zhang at the Oak Ridge National Laboratory and Dr. J. R. Sun at the Institute of Physics of CAS for fruitful discussions. This work was supported by the National Basic Research Program of China under Grant No.2009CB929201, the National Natural Science Foundation of China under Grant Nos.51171205, 51021061 and 50831002, and the US NSF grant DMR-0520491. The use of the Advanced Photon Source at the Argonne National Laboratory is supported by the U.S. DOE under Contract No.DE-AC02-06CH11357.

Correspondence Authors:

*jwcai@iphy.ac.cn

† Li.Sun@mail.uh.edu

References

[1] M. I. D'Yakonov and V. I. Perel, Phys. Lett. A **35**, 459(1971)
[2] J. E. Hirsch, Phys. Rev. Lett. **83**, 1834 (1999).
[3] Y. K. Kato, R. C. Myers, A. C. Gossard, and D. D. Awschalom, Science **306**, 1910 (2004).
[4] F. J. Jedema, H. B. Heersche, A. T. Filip, J. J. A. Baselmans, and B. J. van Wees, Nature **416**, 713 (2002)
[5] S. O. Valenzuela and M. Tinkham, Nature **442**, 176 (2006).
[6] K. Ando, Y. Kajiwara, S. Takahashi, S. Maekawa, K. Takemoto, M. Takatsu, and E.Saitoh, Phys. Rev. B **78**, 014413 (2008).
[7] E. Saitoh, M. Ueda, H. Miyajima, and G. Tatara, Appl. Phys. Lett. **88**, 182509 (2006).
[8] N. E. Christensen, J. Phys. F: Metal Phys. **8**, L51 (1978).
[9] L. Q. Liu, C. F. Pai, Y. Li, H. W. Tseng, D. C. Ralph and R. A. Buhrman, Science 336, 555(2012)
[10] G. E. W. Bauer, E. Saitoh, and B. J. van Wees, Nature Mater. **11**, 391 (2012).

[11] K. Uchida, S. Takahashi, K. Harii, J. Ieda, W. Koshibae, K. Ando, S. Maekawa, and E. Saitoh, Nature **455**, 778 (2008).
[12] Y. Kajiwara, K. Harii, S. Takahashi, J. Ohe, K. Uchida, M. Mizuguchi, H. Umezawa, H. Kawai, K. Ando, K. Takanashi, S. Maekawa, and E. Saitoh, Nature (London) 464, 262 (2010).
[13] I. M. Miron, K. Garello, G. Gaudin, P. J. Zermattern, M. V. Costache, S. Auffret, S. Bandiera, B. Rodmacq, A. Schuhl, and P. Gambardella, Nature 476, 189(2011)
[14] L. Q. Liu, T. Moriyama, D. C. Ralph, and R. A. Buhrman, Phys. Rev. Lett. **106**, 036601 (2011).
[15] S. Y. Huang, X. Fan, D. Qu, Y. P. Chen, W. G. Wang, J. Wu, T. Y. Chen, J. Q. Xiao, and C. L. Chien, Phys. Rev. Lett. **109**, 107204 (2012).
[16] M. Weiler, M. Althammer, F. D. Czeschka, H. Huebl, M. S. Wagner, M. Opel, Inga-Mareen Imort, G. Reiss, A. Thomas, R. Gross, and S. T. B. Goennenwein, Phys. Rev. Lett. **108**, 106602 (2012).
[17] S. Rüegg, G. Schütz, P. Fischer, R. Wienke, W. B. Zeper and H. Ebert, J. Appl. Phys. **69**, 5655 (1991).
[18] W. J. Antel, Jr. M. M. Schwickert, Tao Lin, W. L. O'Brien, and G. R. Harp, Phys. Rev. B **60**, 12933 (1999).
[19] F. Wilhelm, P. Poulopoulos, G. Ceballos, H. Wende, K. Baberschke, P. Srivastava, D. Benea, H. Ebert, M. Angelakeris, N. K. Flevaris, D. Niarchos, A. Rogalev, and N. B. Brookes, Phys. Rev. Lett. 85, 413 (2000).
[20] S. Geprägs, S. Meyer, S. Altmannshofer, M. Opel, F. Wihelm, A. Rogalev, R. Gross and S. T. B. Goennenwein, Cond-mat. Mtrl-sci 1211, 0916 (2012).
[21] M. Susuki, H. Muraoka, Y. Inaba, H. Miyagawa, N. Kawamura, T. Shimatsu, H. Maruyanma, N. Ishimatsu, Y. Isohama, and Y. Sonobe, Phys. Rev. B **72**, 054420(2005)
[22] C. Antoniak, J. Lindner, M. Spasova, D. Sudfeld, M. Acet, M. Farle, K. Fauth, U. Wiedwald, H.-G. Boyen, P. Ziemann, F. Wilhelm, A. Rogalev, and S. Sun, Phys. Rev. Lett. **97**, 117201(2006)
[23] F. Wilhelm, P. Poulopoulos, G. Ceballos, H. Wende, K. Baberschke, P. Srivastava, D. Benea, H. Ebert, M. Angelakeris, N. K. Flevaris, D. Niarchos, A. Rogalev, and N. B. Brookes, Phys. Rev. Lett. **85**, 413 (2000).
[24] B. T. Thole, P. Carra, F. Sette, and G. van der Laan, Phys. Rev. Lett. **68**, 1943 (1992).
[25] P. Carra, B. T. Thole, M. Altarelli, and X. Wang, Phys. Rev. Lett. 70, 694 (1993).
[26] D. Qu, S.Y. Huang, J. Hu, R. Q. Wu, and C. L. Chien, Phys. Rev. Lett. 110, 067206 (2013)

Figure captions

FIG.1 (a) AFM surface topography of a representative YIG film and (b) corresponding room temperature in-plane and perpendicular *M-H* curves. The inset shows the temperature dependence of the YIG spontaneous magnetization.

FIG. 2. (a) Normalized synchrotron x-ray absorption spectra (XAS), and (b) corresponding x-ray magnetic dichroism (XMCD) with an in-plane magnetic field of ±500 Oe from the YIG/Pt(1.5 nm) at 300 K and 20 K. Inset compares the first derivative of the XAS spectra with the XMCD signal. Error bars are included in the XMCD results to indicate measurement noise level.

FIG. 3. (a) Longitudinal and transverse MR curves of a YIG/Pt(1.5 nm) sample measured at 300 K and 5 K with electrode configuration shown in the inset; (b) and (c) coupled MR and Nernst effect measurements for a YIG/Pt(4.0 nm) sample; and (d) Pt thickness dependence of AMR ratio for YIG/Pt at 300 K and 5 K. The solid lines are guides for the eye. Inset in figure (d) plots the resistivity as a function of in-plane field direction (8 kOe) for a representative sample YIG/Pt(1.5 nm) at 300 K, and the solid line is a fitting result using cosine square function.

FIG. 4. (a) Temperature dependence of the anisotropic magnetoresistance for a YIG/Pt(1.5 nm) and a YIG/Pt(4 nm) film; (b) Comparison of the thickness dependent Pt thin film resistivity grown on YIG and GGG substrates as a function of temperature; and (c) ordinary Hall coefficient measured for Pt films grown on YIG and GGG substrates.

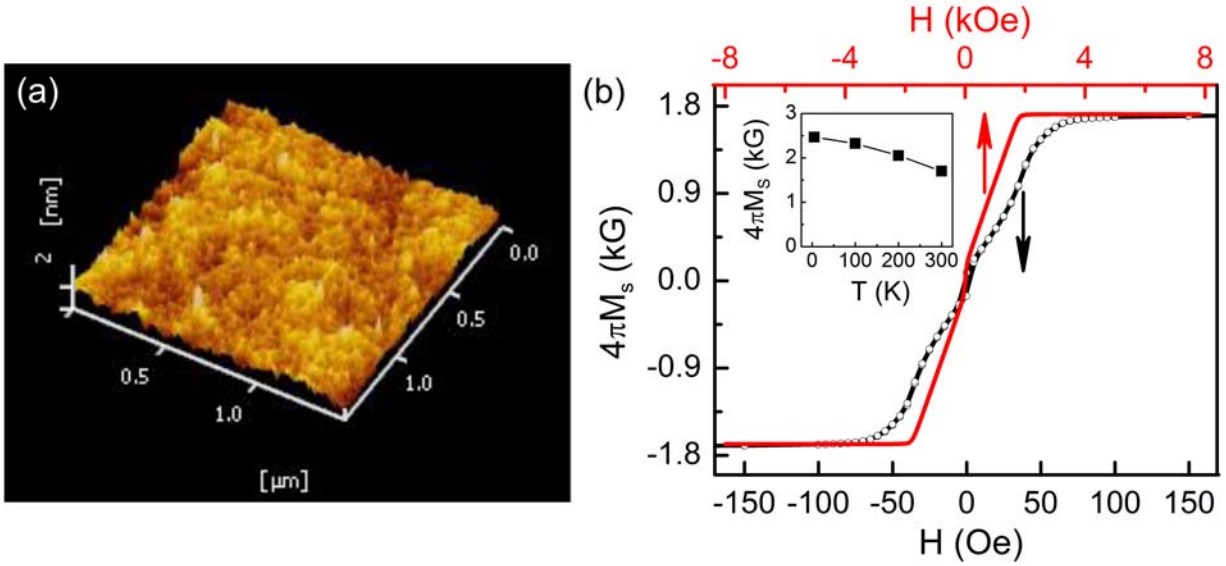
(a)
[nm]
2
0.5
1.0
[μm]
0.0
0.5
1.0
(b)
H (kOe)
-8
-4
0
4
8
1.8
0.9
0.0
-0.9
-1.8
4πM_s (kG)
-150 -100 -50 0 50 100 150
H (Oe)
4πM_S (kG)
3
2
1
0
0 100 200 300
T (K)

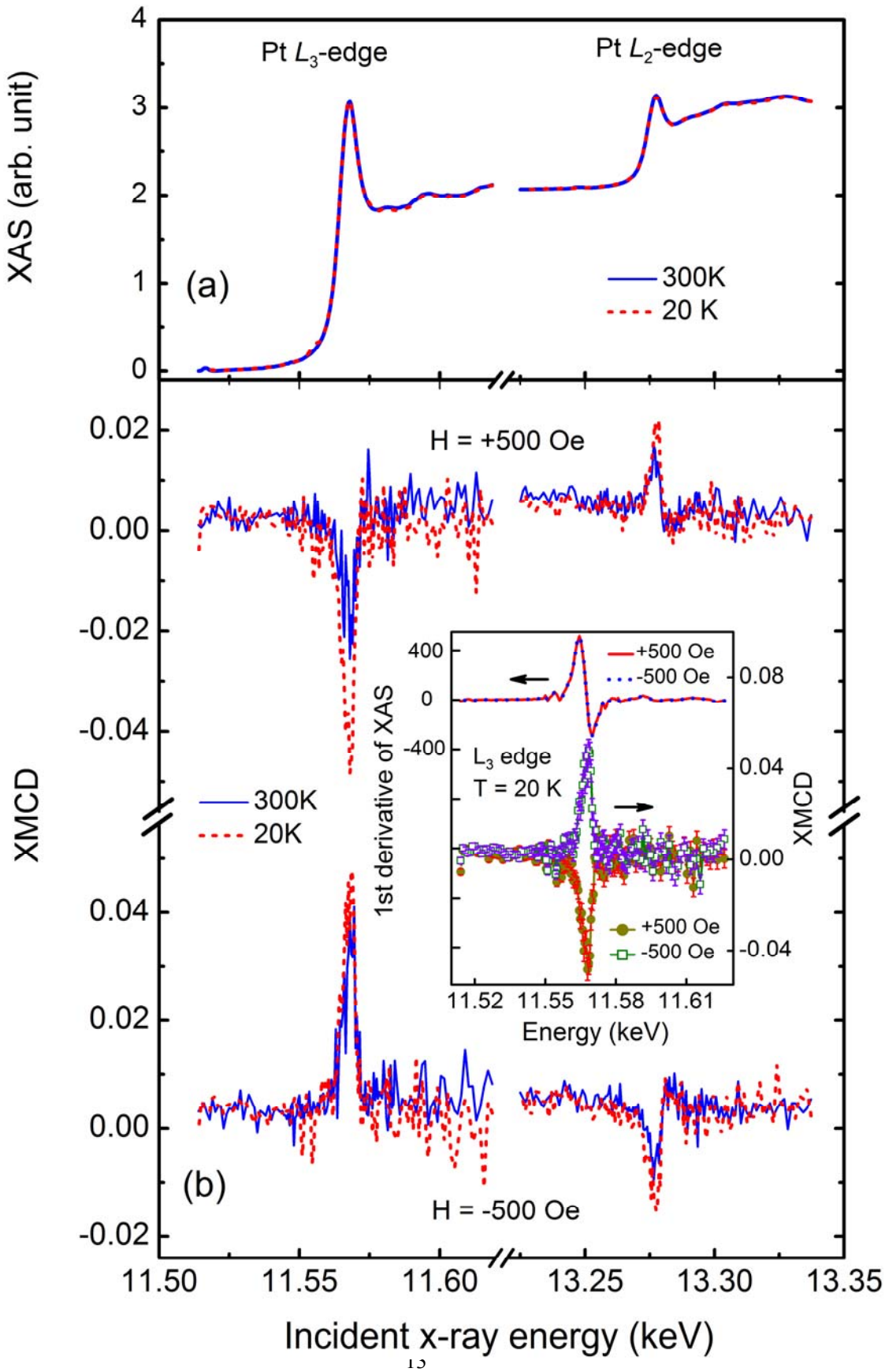
Pt L_3-edge
Pt L_2-edge
XAS (arb. unit)
(a)
300K
20 K
H = +500 Oe
XMCD
300K
20K
H = -500 Oe
(b)
1st derivative of XAS
+500 Oe
-500 Oe
L_3 edge
T = 20 K
Energy (keV)
Incident x-ray energy (keV)

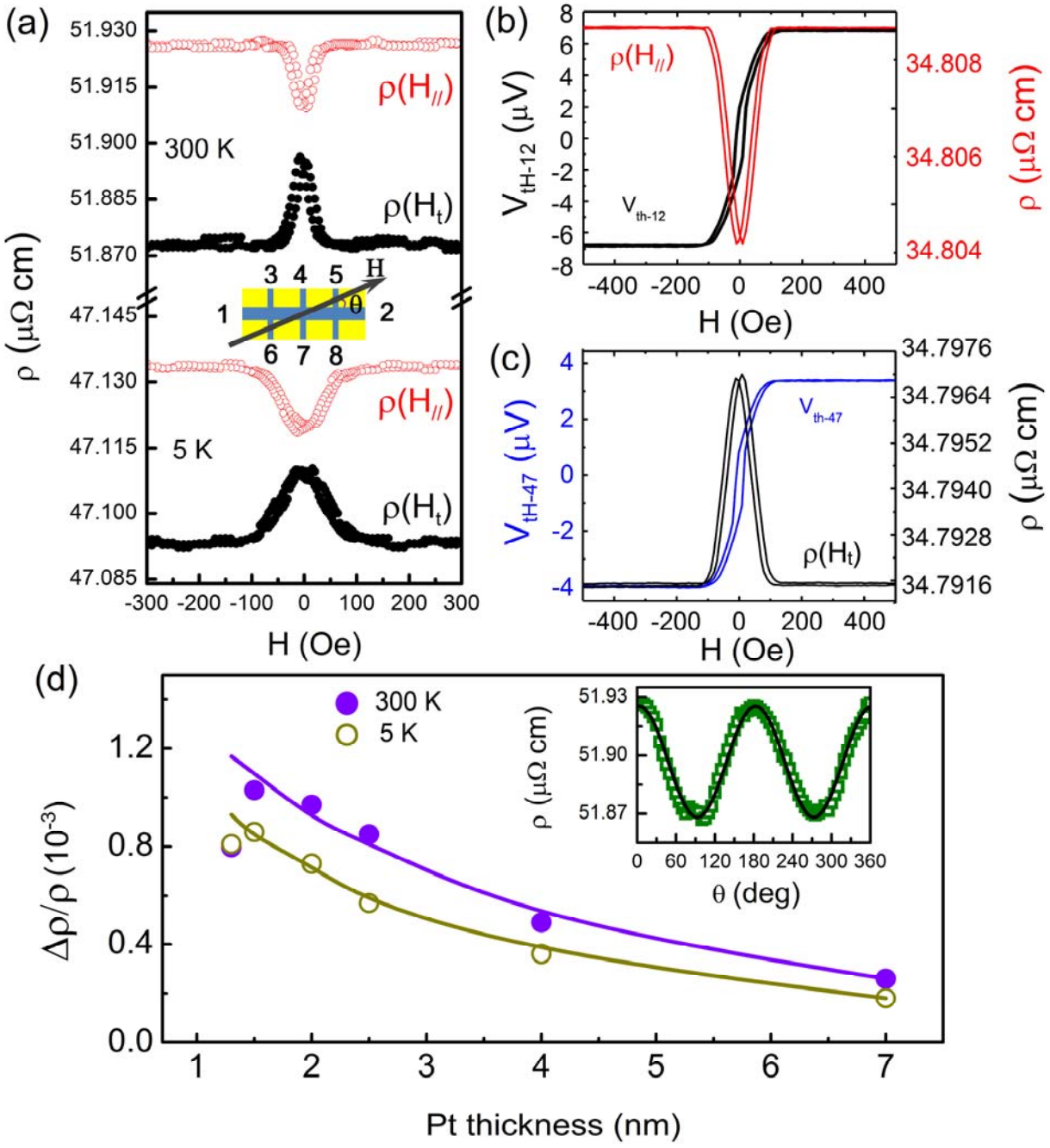
(a)
51.930
51.915
51.900
51.885
51.870
47.145
47.130
47.115
47.100
47.085
ρ (μΩ cm)
ρ(H//)
300 K
ρ(Ht)
3 4 5 H
1 θ 2
6 7 8
ρ(H//)
5 K
ρ(Ht)
-300 -200 -100 0 100 200 300
H (Oe)
(b)
8 6 4 2 0 -2 -4 -6 -8
VtH-12 (μV)
ρ(H//)
Vth-12
34.808
34.806
34.804
ρ (μΩ cm)
-400 -200 0 200 400
H (Oe)
(c)
4 2 0 -2 -4
VtH-47 (μV)
Vth-47
ρ(Ht)
34.7976
34.7964
34.7952
34.7940
34.7928
34.7916
ρ (μΩ cm)
-400 -200 0 200 400
H (Oe)
(d)
300 K
5 K
1.2
0.8
0.4
0.0
Δρ/ρ (10-3)
1 2 3 4 5 6 7
Pt thickness (nm)
51.93
51.90
51.87
ρ (μΩ cm)
0 60 120 180 240 300 360
θ (deg)

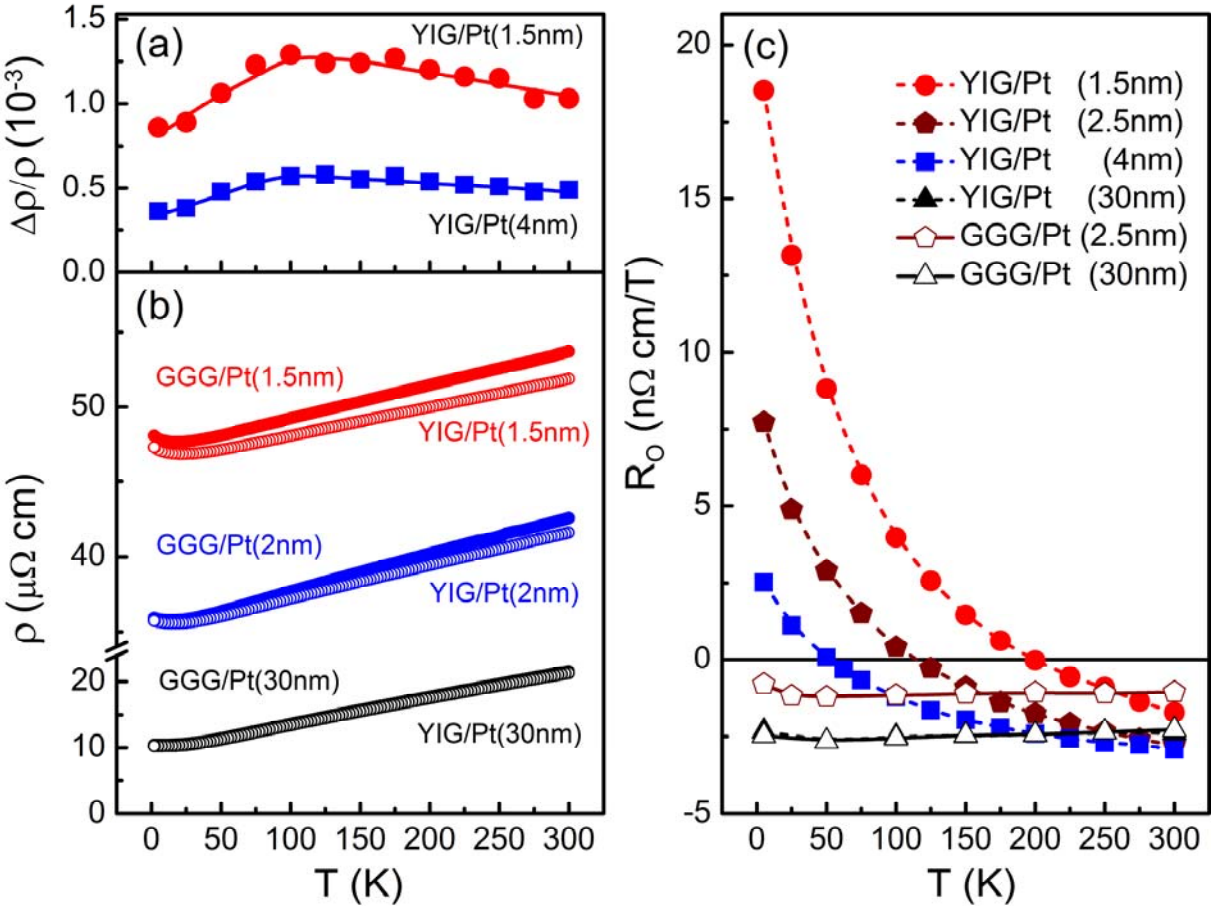
(a)
YIG/Pt(1.5nm)
YIG/Pt(4nm)
Δρ/ρ (10-3)
(b)
GGG/Pt(1.5nm)
YIG/Pt(1.5nm)
GGG/Pt(2nm)
YIG/Pt(2nm)
GGG/Pt(30nm)
YIG/Pt(30nm)
ρ (μΩ cm)
T (K)
(c)
YIG/Pt (1.5nm)
YIG/Pt (2.5nm)
YIG/Pt (4nm)
YIG/Pt (30nm)
GGG/Pt (2.5nm)
GGG/Pt (30nm)
RO (nΩ cm/T)
T (K)